Dual Inhibition of PIK3C3 and FGFR as a New Therapeutic Approach to Treat Bladder Cancer

Chun-Han Chen[1], Chun A. Changou[2,3,4], Tsung-Han Hsieh[5], Yu-Ching Lee[6], Cheng-Ying Chu[6], Kai-Cheng Hsu[2], Hao-Ching Wang[3], Yu-Chen Lin[1], Yan-Ni Lo[6], Yun-Ru Liu[5], Jing-Ping Liou[7], and Yun Yen[2]

Abstract

Purpose: MPT0L145 has been developed as a FGFR inhibitor exhibiting significant anti-bladder cancer activity *in vitro* and *in vivo* via promoting autophagy-dependent cell death. Here, we aim to elucidate the underlying mechanisms.

Experimental Design: Autophagy flux, morphology, and intracellular organelles were evaluated by Western blotting, transmission electron microscope, and fluorescence microscope. Molecular docking and surface plasmon resonance assay were performed to identify drug–protein interaction. Lentiviral delivery of cDNA or shRNA and CRISPR/Cas9-mediated genome editing was used to modulate gene expression. Mitochondrial oxygen consumption rate was measured by a Seahorse XFe24 extracellular flux analyzer, and ROS level was measured by flow cytometry.

Results: MPT0L145 persistently increased incomplete autophagy and phase-lucent vacuoles at the perinuclear region, which were identified as enlarged and alkalinized late-endosomes.

Screening of a panel of lipid kinases revealed that MPT0L145 strongly inhibits PIK3C3 with a K_d value of 0.53 nmol/L. Ectopic expression of PIK3C3 reversed MPT0L145-increased cell death and incomplete autophagy. Four residues (Y670, F684, I760, D761) at the ATP-binding site of PIK3C3 are important for the binding of MPT0L145. In addition, MPT0L145 promotes mitochondrial dysfunction, ROS production, and DNA damage, which may in part, contribute to cell death. ATG5-knockout rescued MPT0L145-induced cell death, suggesting simultaneous induction of autophagy is crucial to its anticancer activity. Finally, our data demonstrated that MPT0L145 is able to overcome cisplatin resistance in bladder cancer cells.

Conclusions: MPT0L145 is a first-in-class PIK3C3/FGFR inhibitor, providing an innovative strategy to design new compounds that increase autophagy, but simultaneously perturb its process to promote bladder cancer cell death. *Clin Cancer Res; 24(5); 1176–89. ©2017 AACR.*

Introduction

Bladder cancer is a common malignancy worldwide (1). In 2017, an estimated 79,030 people will be diagnosed with bladder cancer, and 16,870 people are expected to die from the disease in the United States (2). Statistically, approximately 70% cases are non—invasive bladder cancers (NMIBC) with a 5-year survival rate of about 90%. The other 30% of cases are muscle invasive bladder cancers (MIBCs), which commonly progress to metastasis with a 5-year survival rate of about 50% (3). For patients with MIBC, treatment options are radical cystectomy with neoadjuvant chemotherapy. Platinum-based chemotherapy has been the standard-of-care in advanced bladder cancer for decades, but non-responsiveness and the development of resistance limit its success in improving outcomes for patients. Currently, immunotherapy by checkpoint blockade is the only second-line therapy for patients in whom first-line chemotherapy cannot control the disease (4). Recent studies have identified several genetic alterations in bladder cancer, but targeted therapy is currently unavailable (3). Therefore, it is urgent to develop novel therapeutic agents for patients with bladder cancer.

Macroautophagy (hereafter referred to as autophagy) is a evolutionarily conserved catabolic mechanism by which cells turn over unnecessary cytoplasmic proteins, pathogens, and damaged organelles, such as mitochondria (5). During autophagy, portions of the cytosol, or organelles are sequestered into double-membrane structures known as autophagosomes, and delivered to the lysosome for degradation and recycling of metabolic precursors (6). This process relieves nutritional starvation and maintains cellular homeostasis (7). Recently, autophagy has emerged as an attractive therapeutic target for treatment of human diseases, including cancer (8, 9). Cancer cells activate autophagy in response to cellular stress or increased metabolic demand, contributing to rapid cell proliferation. Moreover, autophagy-related stress tolerance results in resistance to chemotherapeutic agents and ionizing radiation (10, 11). Importantly, autophagy is

[1]Department of Pharmacology, School of Medicine, College of Medicine, Taipei Medical University, Taipei, Taiwan. [2]The Ph.D. Program for Cancer Biology and Drug Discovery, College of Medical Science and Technology, Taipei Medical University, Taipei, Taiwan. [3]Graduate Institute of Translational Medicine, Taipei Medical University, Taipei, Taiwan. [4]Integrated Laboratory, Center of Translational Medicine, Taipei Medical University, Taipei, Taiwan. [5]Joint Biobank, Office of Human Research, Taipei Medical University, Taipei, Taiwan. [6]Research Center of Cancer Translational Medicine, Taipei Medical University, Taipei, Taiwan. [7]School of Pharmacy, College of Pharmacy, Taipei Medical University, Taipei, Taiwan.

AACR

Translational Relevance

Bladder cancer is a common malignancy worldwide, but targeted therapy other than immune checkpoint inhibitors is currently unavailable. MPT0L145 has been developed as a selective FGFR inhibitor exhibiting potent anti-bladder cancer activity *in vitro* and *in vivo* by promoting autophagy-dependent cell death. This study demonstrated that MPT0L145 is a first-in-class PIK3C3/FGFR inhibitor, which not only enhances autophagosome formation (via FGFR inhibition), but also impairs autophagy flux (via PIK3C3 inhibition). Mechanistically, dual inhibition of PIK3C3 and FGFR increases cytoplasmic vacuolization, which promotes mitochondrial dysfunction, ROS production, and DNA damage, contributing to MPT0L145-mediated cell death. Importantly, ATG5-knockout rescued MPT0L145-induced cell death, suggesting simultaneous induction of autophagy is beneficial to the anticancer activity of PIK3C3 inhibitors. Our data demonstrated that MPT0L145 is able overcome cisplatin resistance in bladder cancer cells. These findings provide an innovative strategy to design dual-activity inhibitors as a novel therapy for patients with bladder cancer.

reportedly related to bladder cancer grade, and inhibition of high basal level of autophagy results in apoptotic cell death (12, 13). Meanwhile, autophagy also contributes to cisplatin resistance in bladder cancer cells (14). Therefore, the discovery of novel autophagy inhibitors should provide therapeutic potential to patients with bladder cancer.

PI3Ks (divided into classes I–III) phosphorylate the 3-hydroxyl group of the inositol ring of phosphatidylinositol (PtdIns) lipid substrates and involve in cell-cycle progression, cell growth, survival and migration, and intracellular vesicular transport (15). PIK3C3, also designated vacuolar protein sorting 34 (VPS34), is the only member of the class III PI3K family. PIK3C3 specifically generates PtdIns3P, which, in turn, recruits proteins containing FYVE or PX domains, thereby initiating various complexes at the membranes of endosomes, phagosomes, and autophagosomes (16, 17). Although pan-PI3K blockers, such as 3-methyladenine (3-MA), wortmannin, and LY294002, have been used as autophagy inhibitors, these compounds show limited potency and less selectivity for PIK3C3 (18, 19). In 2010, Miller and colleagues reported the structure of PIK3C3, providing new insights into its catalytic mechanism and underpinning the development of new potent and selective PIK3C3 inhibitors (20, 21). To date, SAR405 has been reported as the most potent selective PIK3C3 inhibitor with a binding equilibrium constant (K_d) of 1.5 nmol/L (22). Studies using SAR405 showed that the catalytic activity of PIK3C3 is necessary for maintaining the size of late endosomes/lysosomes and function of lysosomes during vesicle trafficking. The compound also inhibits autophagy induced by nutrient starvation or mTOR inhibition (23). These results support the potential utility of PIK3C3 as a target for cancer therapy.

Previously, we identified MPT0L145 as a novel FGFR inhibitor with potent anti-bladder cancer activity *in vitro* and *in vivo* (24). MPT0L145 induced nonapoptotic and nonsenescent but autophagy-related cell death. In this study, increases in translucent vacuoles at the peri-nuclear region and accumulation of autophagy substrates, p62 and NDP52, were observed in cells exposed to MPT0L145, implying incomplete autophagy. However, the known specific FGFR inhibitor, BGJ398, exerted no such effects. Accordingly, we hypothesized that dual targets of MPT0L145 may exist. Herein, we aim to elucidate the underlying mechanisms of MPT0L145-induced cell death.

Materials and Methods

Cell culture, antibodies, and reagents

Cisplatin-resistant bladder cancer cell line, N/P (14), was a gift from Dr. Tzyh-Chyuan Hour (Kaohsiung Medical University) (25), and CWR22Rv1-GFP-LC3 cells was from Dr. Hsing-Jien Kung in 2015 (Taipei Medical University) (26). RT-112 and RT-4 cells were purchased and cultured as previously described (24), and were not further authenticated by us. The passage number of each cell line was below 10, and mycoplasma contamination was tested monthly by PCR analysis. MPT0L145 was synthesized by J.-P. Liou according to a previously described protocol (24) and covered by PCT/US2016/043203 filed on July 20, 2016. BGJ398, cisplatin, and 3-MA were acquired from Sellekchem. SAR405 was purchased from AOBIOUS. BLZ945 was purchased from MedChem Express. Cisplatin and rapamycin were purchased from Cayman Chemical. All other chemical reagents were obtained from Sigma Chemical Corp. Antibodies against various proteins were obtained from the following sources: ATG5 (#12994), and γH2AX (#9718) from Cell Signaling Technology and LC3B (#127375), NDP52 (#115378), p62 (#100685), PIK3C3 (#129528), and GAPDH (#100118) from Genetex.

Generation of ATG5 knockout cell line using the CRISPR/Cas9-mediated genome editing

The second coding exon of ATG5 gene (NM_004849) was selected for sgRNA design, and pAll-Cas9.pPpuro and pSurrogate reporter plasmid were purchased from National RNAi Core Facility (Academia Sinica, Taipei, Taiwan). The sgRNA was located behind an U6 promoter of pAll-Cas9.pPpuro plasmid containing the following sequence 5′-AAGATGTGCTTCGAGATGTGTGG-3′. To mimic sgRNA targeting, the region of sgRNA including PAM sequence was cloned into pSurrogate reporter plasmid between EGFP and mCherry CDS. RT-112 cells were seeded into 6-well plate and transfected with sgRNA plasmid and Surrogate reporter plasmid by Lipofectamine 3000 (Thermo Fisher Scientific). After 48 hours, transfected cells were sorted with mCherry fluorescence by Becton Dickinson FACSAria III cell sorter. Viable cells were limiting diluted into a 96-well plate for isolation of single cell clones.

Cell viability and LDH assay

Cells were seeded in 96-well plates and treated with DMSO or the indicated compounds for 72 hours. Cell viability was measured with the MTT assay as described previously (24). For LDH assay, cells were seeded in 96-well plates and treated with drugs at indicated concentrations for 72 hours, followed by measuring lactate dehydrogenase (LDH) release in culture media by using the CytoTox 96 Non-Radioactive Cytotoxicity Assay Kit (Promega) according to the manufacturer's protocol.

Lipid kinase profiling of MPT0L145

The inhibitory activities of MPT0L145 on a panel of lipid kinases were assessed using the service of KINOMEscan

(DiscoverRx). K_d values were determined as described previously (24).

Flow cytometric analysis

Cells were seeded in six-well plates, exposed to DMSO or the indicated compounds for specified times, and harvested via trypsinization. For total cell ROS analysis, cells were stained with 0.1 µmol/L H_2DCFDA (Biotium) at 37°C for 20 minutes. For mitochondrial ROS analysis, cells were stained with 5 µmol/L MitoSOX Red (Thermo Fisher Scientific) at 37°C for 10 minutes. After washing with PBS three times, cells were subjected to ROS detection via flow cytometry with CellQuest software according to the manufacturer's instructions (Becton Dickinson).

Western blot analysis and lentivirus expression system

Cells were seeded in six-well plates and exposed to compounds at various concentrations for the indicated times. After treatment, equal amounts of protein were separated via SDS-PAGE and immunoblotted with specific antibodies, as described previously (24). Lentiviral shRNA expression plasmids of shPIK3C3 (TRCN0000296101, TRCN0000310259) were purchased from the National RNAi Core Facility (Academia Sinica). For PIK3C3 overexpression, a cDNA clone of human PIK3C3 in pcDNA3.1 was purchased from Genscript and lentivirus expression plasmid, pLenti4-PIK3C3, was constructed by inserting full-length PIK3C3 amplified using pairs of primers (5′-TATGTCGACATGGGG-GAAGCAGAGAAGTT-3′ and 5′-TATGAATTCTTAT CACT-TATCGTCGTCATC-3′) into SalI and EcoRI site of pLenti4 expression vector (Invitrogen).

Microscopic image acquisition

For phase-contrast image acquisition, MPT0L145-treated cells were imaged with the EVOS XL Core Cell Imaging System (Thermo Scientific). For fluorescence confocal microscopy, CWR22Rv1-GFP-LC3 cells were seeded in a 35-mm glass-bottomed dish and exposed to MPT0L145. The cells were stained with ER tracker or Lyso tracker (Thermo Scientific) according to the manufacturer's instructions, and live cell images were obtained under a laser scanning confocal fluorescence microscope (Leica TCS SP5). For deconvolution microscopy, CWR22Rv1-GFP-LC3 and RT-112 cells were seeded in a 35-mm glass-bottomed dish and transiently transfected with CellLight Late Endosomes-RFP (Thermo Scientific) for 16 hours. RT-112 cells were additionally stained with pHrodo Green Dextran according to the manufacturer's instructions (Thermo Scientific). These cells were treated with MPT0L145 and the images were obtained using a DeltaVision deconvolution microscope (GE Healthcare) equipped with 60×/1.42 N.A. oil-immersion objective lens. Stacks of optical section images were collected for all fluorochromes, deconvoluted using SoftWorX software, and analyzed with VoloCITY software (PerkinElmer), as described previously (26).

Transmission electron microscopy

MPT0L145-treated cells were fixed in solution containing 2% paraformaldehyde, 2.5% glutaraldehyde, and 0.1 mol/L sodium cacodylate for 1 hour. Fixed cells were washed three times with 0.1 mol/L sodium cacodylate and suspended in buffered solution containing 1% osmic acid for 1 hour. Samples were washed three times with 0.1 mol/L sodium cacodylate followed by dehydration in a graded ethanol series, washed with acetone, and embedded

into EPON epoxy resin. Ultrathin sections (60–80 nm) were prepared using an ultramicrotome and double-stained with uranyl acetate and lead citrate. Samples were examined and images obtained under a Hitachi HT-7700 transmission electron microscope.

Oxygen consumption rate

Cellular mitochondrial function was measured by using a Seahorse XFe24 Extracellular Flux Analyzer and a Seahorse XF Cell Mito Stress Test Kit (Agilent Technologies). The mitochondrial function was examined by directly measuring the oxygen consumption rate (OCR) of cells according to the manufacturer's instructions as described previously (26). Briefly, the cells were seeded onto 24-well plates and treated by MPT0L145 (2 µmol/L) for 48 or 72 hours. After replacing the culture medium to seahorse buffer, oligomycin (1 µmol/L), FCCP (0.5 µmol/L in RT-112 cells and 2 µmol/L in RT-4 cells), and rotenone/antimycin A (0.5 µmol/L) was automatically injected. After finishing recording, OCR values were calculated after normalizing with total protein amounts and plotted as the mean ± SD.

Molecular docking

The PIK3C3 structure (PDB code 4OYS) complexed with SAR405 was downloaded from Protein Data Bank. The binding site of PIK3C3 was defined by residues located ≤10 Å from SAR405. 3D structures of PIK3C3, SAR405, and ATP were generated with ACD/ChemSketch. Compounds were docked onto the binding site using our in-house docking program iGEMDOCK (27). In the docking process, formal charge and atom type (i.e., donor, acceptor, both or nonpolar) of individual atoms of compounds and proteins were assigned using iGEMDOCK. An energy-based scoring function, piecewise linear potential, was used to calculate intermolecular interaction energy between the protein and docked compounds. Finally, iGEMDOCK outputted an interaction profile, including electrostatic, van der Waals, and hydrogen bonding interactions.

Surface plasmon resonance

The cDNA clones of human PIK3C3 or its mutant types (D761A, F684A, I760A, Y670A) in pcDNA3.1 were purchased from Genscript and cloned into the pET-28 expression vector (Novagen). The resultant plasmids were transformed into the *Escherichia coli* BL-21 (DE3) strain for protein expression. Clones were grown in 2YT medium containing kanamycin (100 g/mL) at 37°C and subjected to His-fused protein purification as previously described (28). PIK3C3 protein and small molecular MPT0L145 binding analysis was performed with an OpenSPR instrument (Nicoya Lifesciences). Briefly, 200 µL of the PIK3C3 wild-type or mutant proteins (100 µg/mL) in TBS buffer was provided as the target and immobilized on a Ni-NTA sensor chip. In operation, the running buffer was PBS (pH 7.4), and a constant flow rate of 20 µL/min was used. The small molecular MPT0L145 was diluted in the running buffer in concentrations of 0 to 20 µmol/L for the experiment. The sensor chip was at a flow rate of 50 µL/min after each injection of the MPT0L145. Finally, the data were recorded and analyzed using Trace Drawer software (Ridgeview Instruments), as recommended by the manufacturer. The kinetic parameters of the interaction of the small molecular MPT0L145 with the wild type or mutant form PIK3C3 were investigated using software TraceDrawer according to a 1:1 binding model.

Statistical analysis

Each experiment was performed at least three times. Data in the bar graph are presented as means ± SD. Means were assessed for statistical differences using the Student t test. P values less than 0.05 were considered significant.

Results

MPT0L145 persistently increases incomplete autophagy in bladder cancer cells

In a previous study, we demonstrated that MPT0L145 persistently increased the LC3B-II level from 4 to 72 hours of treatment (24). To ascertain the underlying mechanism, autophagy flux was examined under conditions where degradation of autophagosomes was blocked with chloroquine. In RT-112 cells, chloroquine treatment increased the LC3B-II level relative to that in control cells representing the basal rate of autophagosome formation (Fig. 1A, lane 4). Incubation with MPT0L145 additionally induced an increase in LC-3II, compared with that in control cells (Fig. 1A, lane 2). MPT0L145 further enhanced the LC3B-II level in the presence of chloroquine, suggesting a promotory effect on the rate of autophagosome formation (Fig. 1A, lane 5). The same phenomenon was observed following treatment with another
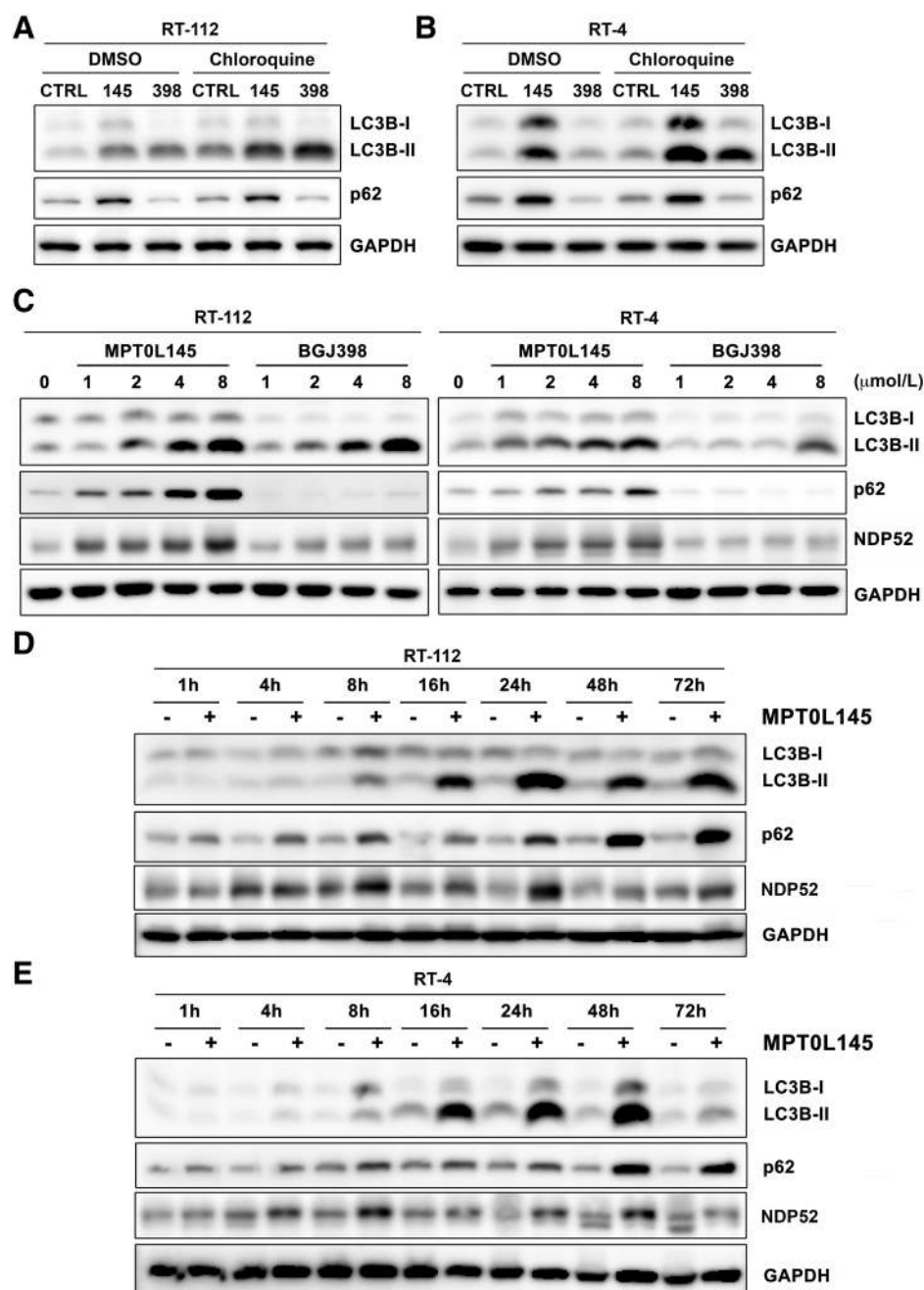
Figure 1.
MPT0L145 persistently increases incomplete autophagy in bladder cancer cells. **A,** RT-112 cells were treated with MPT0L145 or BGJ398 (4 μmol/L) in the presence or absence of chloroquine (25 μmol/L) for 24 hours, and levels of LC3B and p62 detected via Western blot analysis. **B,** RT-4 cells were treated with MPT0L145 or BGJ398 (4 μmol/L) in the presence or absence of chloroquine (3.125 μmol/L) for 24 hours, and levels of LC3B and p62 detected via Western blot analysis. **C,** RT-112 (left) and RT-4 (right) cells were exposed to the indicated concentrations of MPT0L145 and BGJ398 for 24 hours. Protein lysates were subjected to Western blot analysis with the indicated antibodies. **D** and **E,** RT-112 (**D**) and RT-4 (**E**) cells were treated with MPT0L145 (4 μmol/L) for the indicated times, and protein levels of LC3B, p62, and NDP52 were assessed via Western blot analysis.
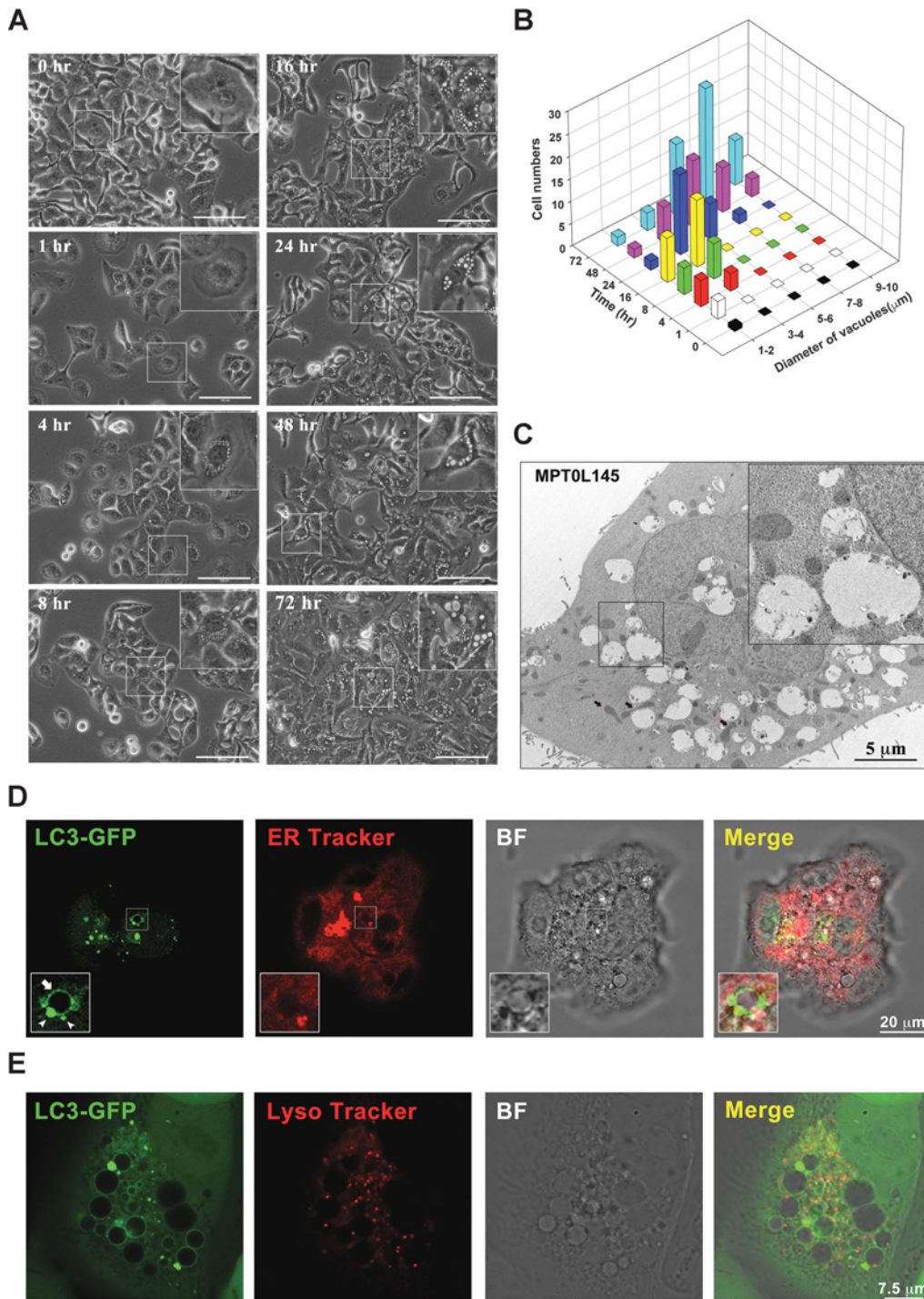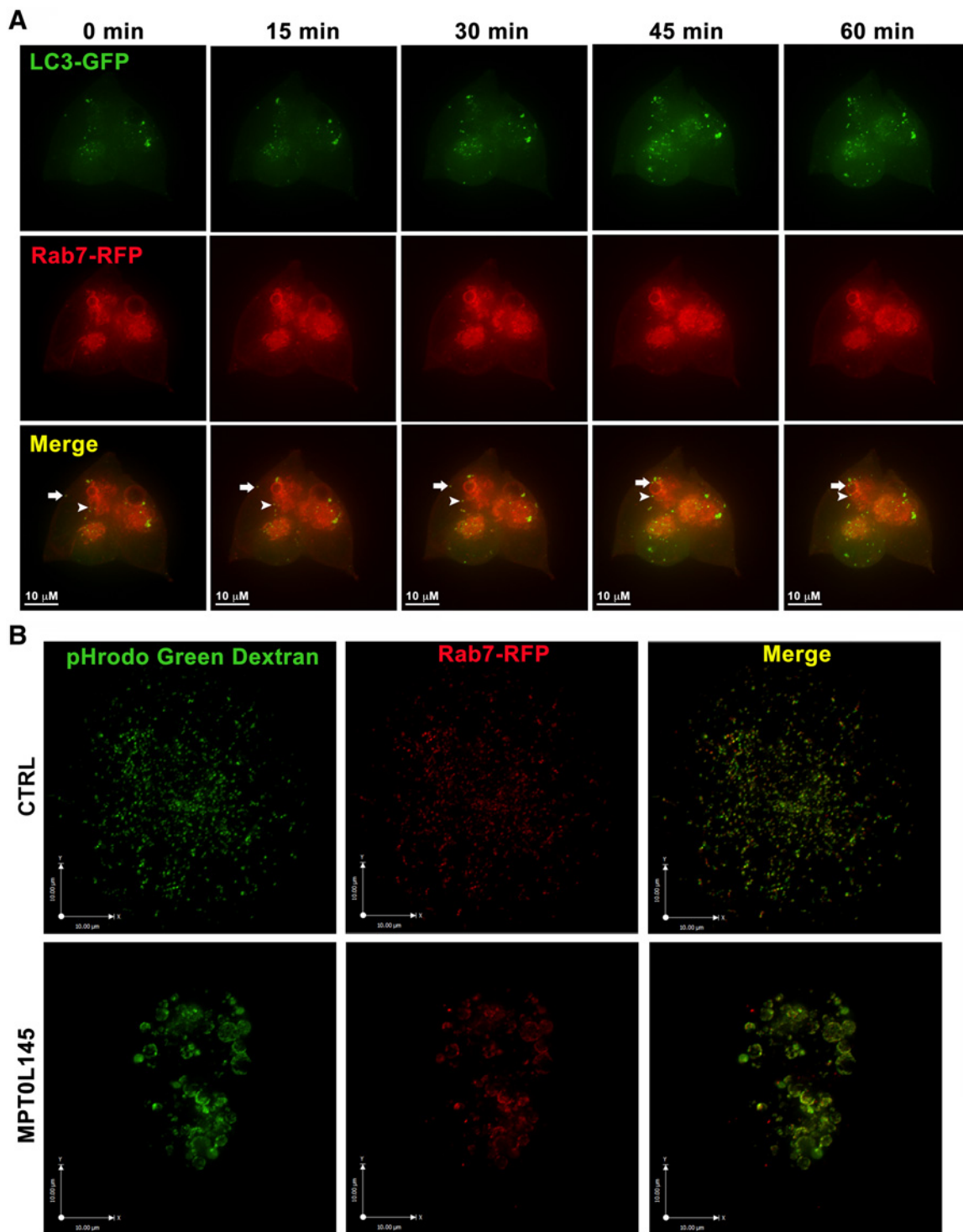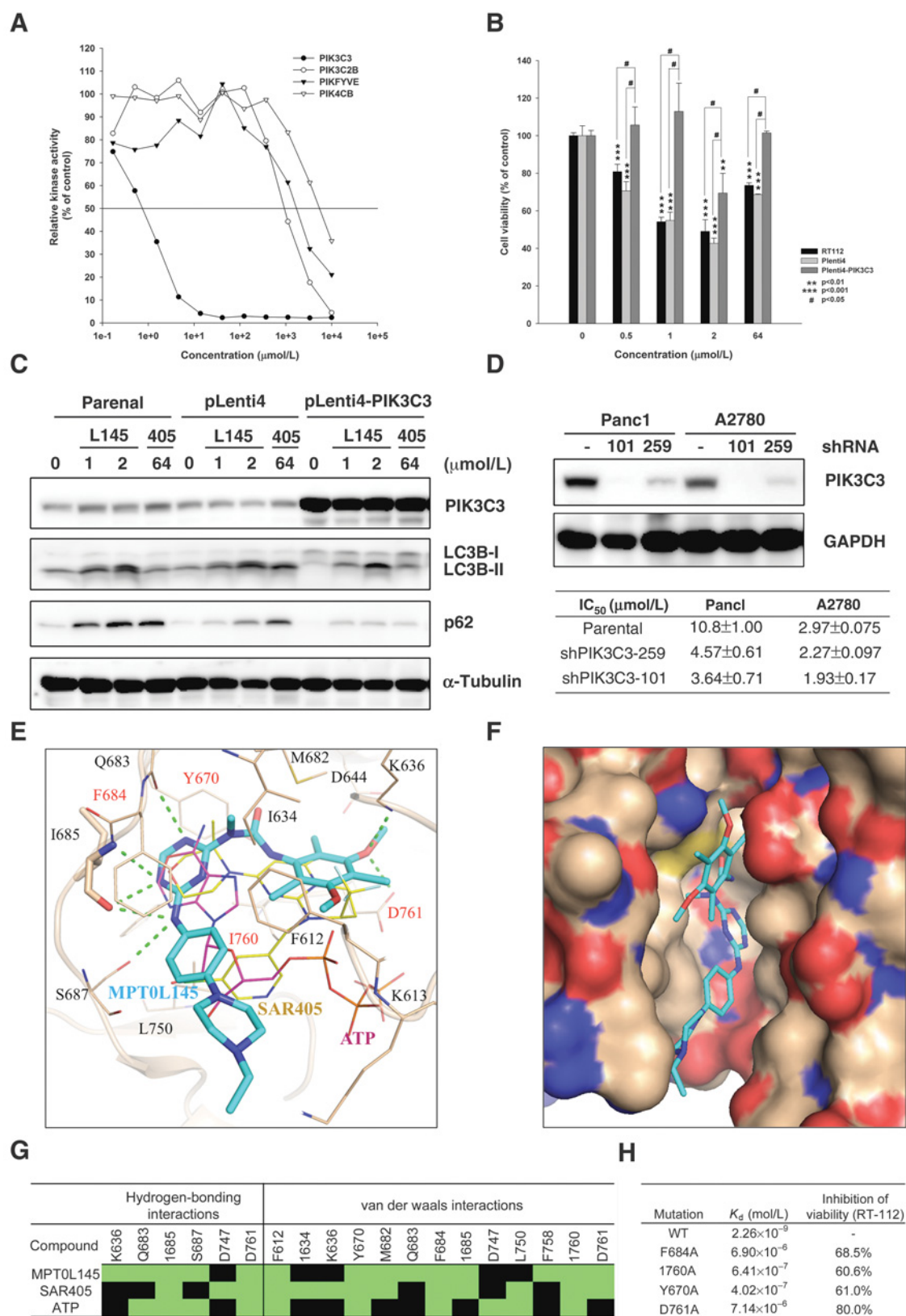
Figure 2.
MPT0L145 induces peri-nuclear vacuolization in RT-112 cells. **A,** RT-112 cells were treated with MPT0L145 (4 μmol/L) for the indicated times and morphology examined under a phase-contrast microscope. Scale bars: 100 μm. **B,** Bar graph depicts the diameter of vacuoles (μm) and numbers of cells at the indicated times in cell lines treated with MPT0L145 (4 μmol/L). **C,** TEM data showing that MPT0L145-induced vacuoles are single membrane structures. No obvious organelles, but some electron-dense matter, were observed within vacuoles (white arrows, with higher magnification in upper right inlet). Swelling of mitochondria was observed (black arrows). Scale bar: 5 μm. **D,** CWR22Rv1 cells stably expressing GFP-LC3 (CWR22Rv1-GFP-LC3, green) were treated with MPT0L145 (4 μmol/L) for 16 hours. Endoplasmic reticulum was labeled with ER tracker (red) at 37°C for 30 minutes before live cell imaging using a confocal microscope. GFP-LC3 puncta were localized on the vacuoles (inset, white arrow heads) and fusion of GFP signal was also observed (inset, white arrow). Scale bars: 20 μm. **E,** CWR22Rv1-GFP-LC3 cells (green) were treated with MPT0L145 (4 μmol/L) for 16 hours. Lysosomes were labeled with LysoTracker (red) at 37°C for 30 minutes before live cell imaging using a confocal microscope. Scale bars: 7.5 μm.

Figure 3.
MPT0L145-induced cytoplasmic vacuoles are enlarged but malfunctioning late endosomes. **A,** CWR22Rv1-GFP-LC3 cells were transiently transduced with Rab7-RFP (red) for 16 hours and subsequently incubated with MPT0L145 (4 μmol/L) for 5 hours. Time-lapse deconvolution microscopy images were obtained for 60 minutes with an interval of 15 minutes between sequential images. The movement of autophagosome toward enlarged late-endosome was observed (white arrow and arrowhead). Scale bars: 10 μm. **B,** RT-112 cells were transiently transduced with Rab7-RFP (red) for 16 hours and incubated with pHrodo Green dextran (10,000 MW) at 37°C for 30 minutes to examine endocytosis function and acidity of late endosomes. After treatment with vehicle (DMSO) or MPT0L145 (4 μmol/L) for 5 hours, live cell images were obtained via deconvolution microscopy. Scale bars: 10 μm.

D

IC$_{50}$ (µmol/L)	Pancl	A2780
Parental	10.8±1.00	2.97±0.075
shPIK3C3-259	4.57±0.61	2.27±0.097
shPIK3C3-101	3.64±0.71	1.93±0.17

H

Mutation	K_d (mol/L)	Inhibition of viability (RT-112)
WT	2.26×10^{-9}	-
F684A	6.90×10^{-6}	68.5%
I760A	6.41×10^{-7}	60.6%
Y670A	4.02×10^{-7}	61.0%
D761A	7.14×10^{-6}	80.0%

FGFR inhibitor, BGJ-398 (Fig. 1A, lane 6). However, the p62 level was enhanced by MPT0L145, distinct from findings with BGJ-398. MPT0L145 enhanced the level of autophagy substrates (p62, NDP52) in a concentration-dependent manner over 24 hours, whereas BGJ398 suppressed their expression (Fig. 1C, left). Time-course analysis demonstrated accumulation of LC-3II, p62, and NDP52 from 4 to 72 hours, reflecting suppression of autophagosome turnover by MPT0L145 (Fig. 1D). In contrast, BGJ398 suppressed p62 expression in a time-dependent manner (Supplementary Fig. S1A). Similar results were observed in RT-4 cells, excluding the possibility of cell-type–specific events (Fig. 1B and C, right and E; Supplementary Fig. S1B). Our data collectively suggest that MPT0L145 not only increases autophagosome formation but also simultaneously disrupts its degradation.

MPT0L145 induces cytoplasmic vacuolization in bladder cancer cells

To gain insights into the mechanisms underlying MPT0L145-related cell death, we examined morphological changes via phase-contrast microscopy. One significant feature was increased phase-lucent vacuoles at the perinuclear region as early as 1 h after treatment with MPT0L145 (Fig. 2A). Notably, vacuoles became larger in a time-dependent manner, ranging from 1 to 10 μm in diameter (Fig. 2B). Transmission electronic microscopy (TEM) further revealed that these vacuoles are electron lucent at the perinuclear region. Notably, vacuoles were single-membrane structures and lacked visible cytoplasmic organelles (with some electron-dense matter), suggesting that they do not represent enlarged autophagosomes (Fig. 2C). MPT0L145-induced vacuolization was also observed in another bladder- (RT-4) or nonbladder (PLC/PRF/5) cancer cells (Supplementary Fig. S1C and S1D). Moreover, enlarged vacuoles with compressed nuclei and abnormal morphology of mitochondria were observed (Fig. 2C). Our findings clearly suggest that MPT0L145 causes accumulation of phase-lucent vacuoles in bladder cancer cells.

MPT0L145-induced cytoplasmic vacuoles are enlarged but malfunctioning late endosomes

Next, we examined the effects of MPT0L145 on organelles adjacent to the nucleus, such as endoplasmic reticulum (ER), lysosomes and late endosomes. CWR22Rv1 cells stably expressing GFP-LC3 in conjunction with different labeling methods were used to determine the localization of autophagosomes and other subcellular compartments. First, we examined the effect of MPT0L145 on autophagosomes and ER using ER tracker. In the presence of MPT0L145, no overlap was observed between

vacuoles and ER (Fig. 2D). Autophagosomes were localized on the surface of vacuoles based on GFP puncta formation and z-axis scanning via confocal microscopy (Fig. 2D; Supplementary Movie S1). Notably, the autophagosome membrane appeared to fuse with vacuoles, represented by a thin-layer distribution of GFP signal on their surface (Fig. 2D). Given the unsuccessful degradation of autophagy substrate (p62), we further investigated the effects of MPT0L145 on lysosomes via LysoTracker. Lysosomes were detected surrounding or on the surface of vacuoles, but no marked fusion of LysoTracker dye was observed (Fig. 2E). Late endosomes are reported to be involved in the process of autophagy (29). Accordingly, Rab7a-RFP was ectopically expressed in cells stably expressing GFP-LC3, followed by exposure to MPT0L145, to ascertain whether these vacuoles are late endosomes. 4D deconvolution microscopy revealed the presence of the RFP signal on the surface of vacuoles and autophagosomes moving towards these vacuoles (Fig. 3A). Our findings collectively indicate that the vacuoles are not autophagosomes, ER or lysosomes, but enlarged late endosomes and their fusion with lysosomes is disrupted by MPT0L145.

Late endosomes are derived from the vacuolar domains of early endosomes, and maturation requires exchange of membrane components, movement to the peri-nuclear area, and acidification of luminal pH (30). Next, we examined the functions of the enlarged late endosomes in MPT0L145-treated RT-112 cells in endocytosis and endosomal function using a fluid phase marker (dextran labeled with pHrodo Green) and obtained 3D images under a deconvolution microscope. Because of its large molecular weight, dextran can only enter cells through endocytosis. Upon internalization, the acidic environment of endosomes induces pHrodo dye emission of green fluorescence from this dextran conjugate. In the control group, we observed significant colocalization of pHrodo Green and Rab7-RFP, suggesting that endocytosis is normal and late endosomes are well acidified (Fig. 3B, top; Supplementary Movie S2). In cells treated with MPT0L145, colocalization of green and red fluorescence could only be detected on the surface of enlarged late endosomes. However, we were unable to detect the fluorescent signal within these vacuoles, suggesting that the center of late endosomes is alkalinized (Fig. 3B, bottom; Supplementary Movie S3). Our data demonstrated that MPT0L145 induces enlarged but malfunctioning late endosomes without affecting endocytosis activity.

MPT0L145 is a potent PIK3C3 inhibitor

We next elucidated the mechanisms underlying MPT0L145-induced vacuolization. MPT0L145 was previously identified as a novel FGFR inhibitor via screening of a panel of protein kinases (24), but another selective FGFR inhibitor, BGJ398, was not able

Figure 4.
MPT0L145 is a potent PIK3C3 inhibitor. **A,** *In vitro* inhibitory effects of MPT0L145 on lipid kinases. *In vitro* inhibitory activities of MPT0L145 were assessed using the service of KINOMEscan (DiscoverRx). Data are represented by percent kinase activity relative to control group with two technical repeats. **B,** RT-112 cells stably expressing pLenti4 vector or pLenti4-PIK3C3 were treated with the indicated concentrations of MPT0L145 or SAR405 (64 μmol/L) for 72 hours, and cell viability measured with the MTT assay. Data are expressed as means ± S.D. (**, $P < 0.01$; ***, $P < 0.001$ compared to the control group; #, $P < 0.05$ compared to parental cells). **C,** RT-112 cells stably expressing pLenti4 vector or pLenti4-PIK3C3 were treated with the indicated concentrations of MPT0L145 or SAR405 (64 μmol/L) for 24 hours. Protein lysates were subjected to Western blot analysis using the indicated antibodies. **D,** PIK3C3 was stably depleted in Panc1 and A2780 cells with two different sequences of shRNA (101, 259). The protein level of PIK3C3 was examined via Western blot analysis (top), and IC_{50} values of MPT0L145 in parental or PIK3C3 knockdown cells were measured by MTT assay (bottom). **E,** Binding conformation of MPT0L145 (cyan). SAR405 (yellow) and ATP (pink) are the reference compounds. Hydrogen bonds between L145 and PIK3C3 are presented as green dashed lines. **F,** Surface representation of PIK3C3 showing the binding conformation of MPT0L145. **G,** Interaction profiles of MPT0L145, SAR405, and ATP. Cells are colored green in case of interactions (hydrogen bonding or van der Waals) between a compound and residue and otherwise colored black. **H,** Effects of PIK3C3 mutations on K_d values and cell viability.
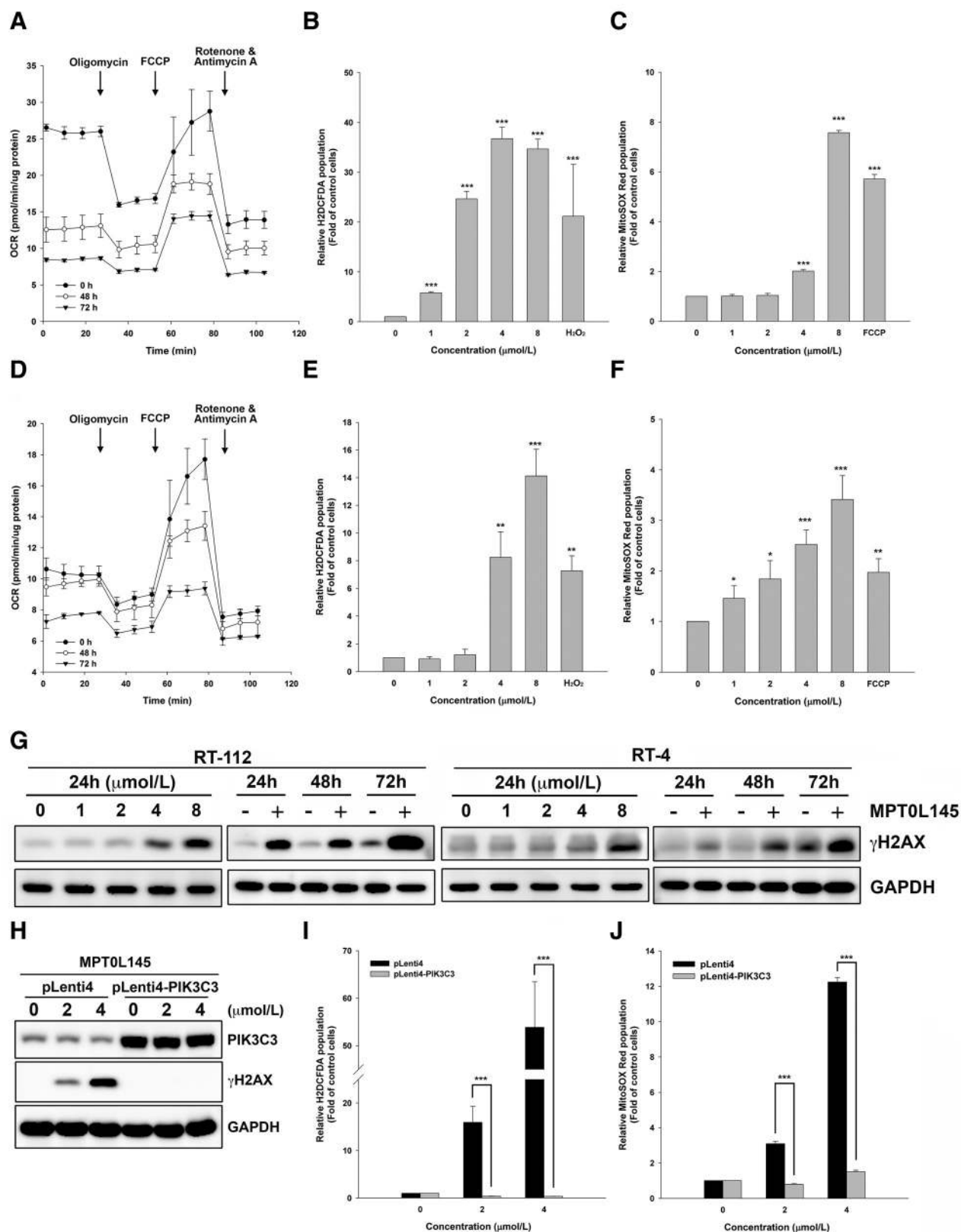
to induce vacuolization (Supplementary Fig. S1E). Therefore, we speculated that there might be a missing target of MPT0L145. Literature to date has shown that lipids control various steps in autophagy and inhibition of specific lipid kinases results in peri-nuclear vacuolization and blockade of endosomal functions (31, 32). Examination of the effects of MPT0L145 on a panel of lipid kinases led to its identification as a highly potent PIK3C3 inhibitor with a K_d value of 0.53 nmol/L showing selectivity from three to four orders of magnitude over other lipid kinases (Fig. 4A; Supplementary Table S1). Currently, SAR405 is reported as the most potent selective inhibitor of PIK3C3 (22, 33). We further compared the *in vitro* kinase inhibition activity of SAR405 under the same conditions, obtaining a K_d value of 46 nmol/L (Supplementary Fig. S2). Thus, we observed that PIK3C3 is a crucial target of MPT0L145 with inhibitory activity in the sub-nanomolar range. Ectopic expression of PIK3C3 reversed the effects of MPT0L145 and SAR405 on cell viability as well as accumulation of p62 in RT-112 cells (Fig. 4B and C). Conversely, knockdown of PIK3C3 via specific shRNA was achieved in Panc1 and A2780 cells, which are resistant to MPT0L145. Compared to parental cells, knockdown of PIK3C3 resulted in differential potentiation of MPT0L145, as evident from decreased IC$_{50}$ values in Panc1 and A2780 cells (Fig. 4D; Supplementary Fig. S3A and S3B). These results support the theory that PIK3C3 is a crucial target of MPT0L145 that contributes to its anticancer activity.

To further confirm our findings, molecular docking analysis was performed to clarify the binding modes of MPT0L145 for PIK3C3. The docking results showed that MPT0L145 inhibits PIK3C3 activity by blocking the ATP-binding site (Fig. 4E and F). MPT0L145 mainly consists of three components: triazine, 1-ethyl-4- phenylpiperazine and 1,3,5-trichloro-2,4-dimethoxy-benzene. The triazine group occupies the same position as the adenine ring of ATP and is sandwiched between two aromatic residues, Y670 and F684. It also forms hydrogen bonds with Q683 and I685 of the hinge region. The second group is located downstream of the hinge region and forms stable van der Waals interactions with two phenylalanine residues, F612 and F684. The 1,3,5-trichloro-2,4-dimethoxybenzene group of MPT0L145 and pyrimidine group of SAR405 bind in the same location (Fig. 4E). This group forms two hydrogen bonds with K636 and D761, a key residue in the DFG motif, and van der Waals contacts with M682 and I760. In addition, the nitrogen atom linked to the first two groups yields two hydrogen bond interactions with I685 and S687. Interaction analysis showed that the main difference

between MPT0L145 and SAR405 is the number of hydrogen bond interactions. MPT0L145 forms additional hydrogen bonds with K636, Q683, I685, and S687. MPT0L145 forms three hydrogen bonds with I685 whereas SAR405 only has one hydrogen bond, potentially accounting for the higher potency of L145 against PIK3C3. Four residues (i.e., Y670, F684, I760, and D761) that form consensus interactions with MPT0L145, SAR405, and ATP (Fig. 4G) were mutated to alanine to examine their importance in compound binding using surface plasmon resonance (SPR) experiments. I685 and F612 were not selected because hydrogen bond interactions occur with their main chains. The data suggested that these mutations decreased the binding of MPT0L145 to PIK3C3 as evidenced by the increase in K_d value by two to three orders of magnitude (Fig. 4H; Supplementary Table S2). Ectopic expression of the mutant proteins resulted in inhibition of cell viability in RT-112 cells, ranging from 60% to 80% (Fig. 4H). Among these residues, D761 was the most essential for the binding of MPT0L145 to PIK3C3. Our results indicate that these four residues play a critical role in molecular recognitions, supporting their utility in the design of PIK3C3 inhibitors.

MPT0L145 promotes mitochondrial dysfunction, ROS generation, and DNA damage

In this study, we identified PIK3C3 as the primary target of MPT0L145, which persistently promotes vacuolization. TEM data revealed the presence of enlarged vacuoles with compressed nuclei and abnormal morphology of mitochondria (Fig. 2C), which led us to speculate that MPT0L145 impairs mitochondrial function in bladder cancer cells. To proof our hypothesis, the mitochondrial OCR was measured in MPT0L145-treated RT-112 cells by a Seahorse XFe24 Extracellular Flux Analyzer. Oligomycin is an inhibitor of mitochondrial ATP synthase, and the decrease in OCR following injection of oligomycin correlates to the mitochondrial respiration associated with cellular ATP production. Carbonyl cyanide-4-(trifluoromethoxy)phenylhydrazone (FCCP) is a proton uncoupler, leading to a rapid consumption of oxygen without the generation of ATP. Hence, the addition of FCCP allowed for an estimation of the maximal respiration. Followed by FCCP, the third injection is a mixture of rotenone (complex I inhibitor) and antimycin A (complex III inhibitor) shunting down whole mitochondrial respiration. Figure 5A reveals that baseline OCR level was suppressed by treatment of MPT0L145 in a time-dependent manner and ATP production was decreased as evident from the lack of response to oligomycin. Moreover, MPT0L145 impaired the maximal respiration as

Figure 5.
Inhibition of PIK3C3 promotes mitochondrial dysfunction, ROS production, and DNA damage in bladder cancer cells. **A** and **D,** Time-dependent effects of MPT0L145 on mitochondrial OCR in RT-112 (**A**) and RT-4 (**D**) were measured using a Seahorse XFe24 Extracellular Flux Analyzer as describe in the section Materials and Methods. **B** and **E,** MPT0L145 increased intracellular ROS level in bladder cancer cells. RT-112 (**B**) and RT-4 (**E**) cells were treated with indicated concentrations of MPT0L145 for 72 hours. Cells in the positive control group were incubated with H_2O_2 (1 μmol/L) for 1 hours. Intracellular ROS levels were measured via flow cytometric detection of the H_2DCFDA population. Data are expressed as means ± SD (**, $P < 0.01$; ***, $P < 0.001$, compared to the control group). **C** and **F,** Effects of MPT0L145 on mitochondrial ROS level in bladder cancer cells. RT-112 (**C**) and RT-4 (**F**) cells were exposed to the indicated concentrations of MPT0L145 for 72 hours. Cells in the positive control group were treated with FCCP (5 μmol/L) for 1 hour. Mitochondrial superoxide was measured by detection of MitoSOX Red-positive cells via flow cytometry. Data are expressed as means ± SD (*, $P < 0.05$; **, $P < 0.01$; ***, $P < 0.001$, compared to the control group). **G,** Effects of MPT0L145 on DNA damage response. RT-112 (left two panels) and RT-4 (right two panels) cells were incubated with the indicated concentrations of MPT0L145 for 24 h or with MPT0L145 (4 μmol/L) for different time periods. Protein lysates were subjected to Western blot analysis for detection of the DNA damage marker, γH2AX. **H–J,** Enforced expression of PIK3C3 rescues the MPT0L145-mediated increase in DNA damage and ROS production. RT-112 cells stably expressing pLenti4 vector or pLenti4-PIK3C3 were treated with the indicated concentrations of MPT0L145 for 72 hours. Protein levels (**H**) of PIK3C3 and γH2AX were examined via Western blot analysis. Intracellular ROS (**I**) and mitochondrial ROS (**J**) were measured based on detection of H_2DCFDA-, and MitoSOX Red-labeled populations via flow cytometry. Data are expressed as means ± SD (***, $P < 0.001$, compared to pLenti4 vector-expressing cells).
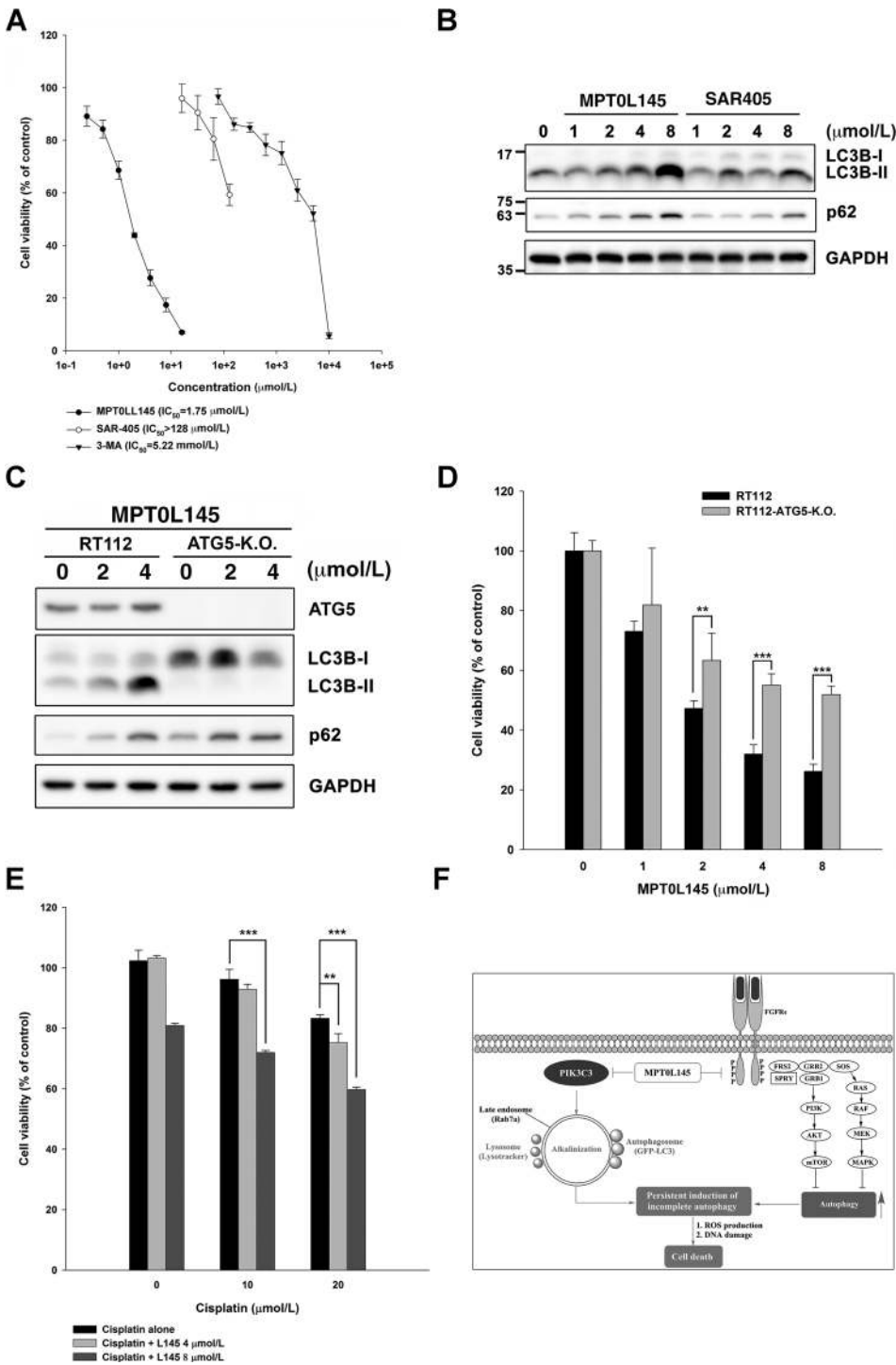
Figure 6.
Induction of autophagy is crucial to the cytotoxicity of MPT0L145. **A,** RT-112 cells were incubated with the indicated concentrations of MPT0L145, SAR405, and 3-methyladenine (3-MA) for 72 hours, and cell viability was examined by MTT assay. Data are expressed as means ± SD. **B,** RT-112 cells were exposed to the indicated concentrations of MPT0L145 and SAR405 for 24 hours, and protein levels of LC3B and p62 evaluated via Western blot analysis. **C,** RT-112 and RT-112-ATG5-K.O. cells were exposed to indicated concentrations of MPT0L145 for 24 hours, and subjected to Western blot analysis. **D,** RT-112 and RT-112-ATG5-K.O. cells were exposed to indicated concentrations of MPT0L145 for 72 hours, and cell viability was examined by MTT assay. Data are expressed as means ± SD. (**, $P < 0.01$; ***, $P < 0.001$ compared to RT-112 cells). **E,** Cisplatin-resistant N/P (14) cells were treated with indicated concentrations of cisplatin in the presence or absence of MPT0L145 for 72 hours, and cell viability was examined by MTT assay. Data are expressed as means ± SD (**, $P < 0.01$; ***, $P < 0.001$ compared to cisplatin alone group). **F,** Proposed mechanism of MPT0L145-induced cell death. We previously identified that MPT0L145 exhibits inhibitory activity against FGFRs and triggers autophagy-related cell death. In current study, we further identified that MPT0L145 is a highly potent PIK3C3 inhibitor, which promotes accumulation of enlarged late endosomes at peri-nuclear region and persistently induces incomplete autophagy, that cause cell death through ROS accumulation and DNA damage.

evident by the lack of response to FCCP (Fig. 5A). Mitochondrial defects reportedly trigger the release of ROS, potentially leading to DNA damage (26). As shown in Fig. 5B, MPT0L145 induced a significant increase in the H_2DCFDA-positive population at 72 hours, suggesting an increase in the intracellular ROS level. MitoSOX staining data verified our speculation of mitochondrial superoxide production (~2- to eightfold higher than the vehicle-

treated group; Fig. 5C). Same phenomenon was observed in MPT0L145-treated RT-4 cells (Fig. 5D–F). In addition, MPT0L145 enhanced the expression of the DNA damage marker, γH2AX, in a concentration-dependent manner after 24 hours of treatment, and the maximum effect occurred at 72 hours of treatment (Fig. 5G). In this study, we observed that ectopic expression of PIK3C3 rescued MPT0L145-induced cell death (Fig. 4B). It

prompts us to examine whether PIK3C3 inhibition contributes to ROS production and DNA damage. The data showed that enforced expression of PIK3C3 rescued the level of DNA damage marker (γH2AX) and intracellular/mitochondrial ROS production (Fig. 5H–J). Cotreatment with ROS scavengers (ebselen, trolox) partially abolished MPT0L145-induced cell death (Supplementary Fig. S3C and S3D). Together, we conclude that the MTP0L145-mediated mitochondrial dysfunction, increase in intracellular/mitochondrial ROS production and DNA damage, at least in part, contributes to cell death.

Induction of autophagy is crucial to the cytotoxicity of MPT0L145

In this study, we observed that MPT0L145 persistently increases incomplete autophagy in RT-112 cells (Fig. 1A). It exhibited stronger cytotoxic activity relative to other PIK3C3 inhibitors, such as SAR405 and 3-MA (Fig. 6A). Meanwhile, MPT0L145 induced greater LC3B-II expression and accumulation of p62 than SAR405 (Fig. 6B). Therefore, we hypothesized that inhibition of PIK3C3 alone is not sufficient to promote bladder cancer cell death, and simultaneous induction of autophagy potentiates the anticancer activity of PIK3C3 inhibitors. To confirm our hypothesis, ATG5-knockout (ATG5-K.O.) RT-112 cells, where no conversion of LC3-I to LC3-II can take place, were generated by CRISPR/Cas9-mediated genome editing. ATG5 knockout cells were confirmed by western blot analysis (Fig. 6C) and DNA sequencing of the genomic regions (Supplementary Fig. S4). The data showed that no appreciable increase in LC3B-II after the treatment of MPT0L145, suggesting lack of autophagy in RT-112-ATG5-K.O. cells (Fig. 6C). Knockout of ATG5 reversed MPT0L145-induced cell death (Fig. 6D). Moreover, cisplatin reportedly induces protective autophagy that causes drug resistance in bladder cancer cells (14). We therefore used cisplatin-resistant N/P (14) generated from human bladder cancer to further proof our concept in the preclinical setting (25). The results revealed that MPT0L145 overcame cisplatin resistance in N/P (14) cells (Fig. 6E). Collectively, our data suggested that simultaneous induction of autophagy is crucial to the cytotoxicity of MPT0L145.

Discussion

Bladder cancer is a common malignancy worldwide, but targeted therapy other than immune checkpoint inhibitors is currently unavailable. Recent studies have identified several genetic alterations in bladder cancer, including the activation of FGFR pathways (3). Previously, we identified MPT0L145 inhibits FGFR1 and FGFR3 with the K_d values of 130 and 270 nmol/L, respectively (24). However, CSF1R was also inhibited by MPT0L145 with the K_d value of 340 nmol/L. As CSF1R is primarily expressed in mononuclear phagocytes (34), and selective CSF1R inhibitor (BLZ945) has no effect on the viability in bladder cancer cells (Supplementary Fig. S5A), the involvement of CSF1R inhibition in MPT0L145-induced cell death could be eliminated. In this study, we observed that MPT0L145 is an even more potent inhibitor of the lipid kinase, PIK3C3, resulting in incomplete autophagy in bladder cancer cells. Recent studies revealed that FGFR antagonist induces protective autophagy, and simultaneously inhibition of FGFR and autophagy could enhance cancer cell death (35, 36). As a result, dual inhibition of FGFR3 and autophagy via PIK3C3

blockade was achieved by MPT0L145 via a concentration-dependent manner (Supplementary Fig. S5B), and no appreciable necrotic effects were observed in bladder cancer cells (Supplementary Fig. S5C). Therefore, we provide an innovative method to discover novel therapy for bladder cancer by showing that MPT0L145 is a first-in-class PIK3C3/FGFR inhibitor, which not only enhances autophagosome formation, but also impairs autophagy flux (Fig. 6F).

SAR405 is reportedly the most potent and selective PIK3C3 inhibitor, which inhibits autophagy induced by nutrient starvation or mTOR inhibition (22). However, SAR405 alone is not sufficiently potent to inhibit growth of renal tumor cells (IC_{40} = 20,816 nmol/L in ACHN and 8,091 nmol/L in 786-O; ref. 23). Thus, it appears that inhibition of PIK3C3 alone may not exert a sufficient cancer killing effect and activation of autophagy may additionally be required for effective antitumor activity. A single compound that increases autophagosome formation and simultaneously inhibits autophagy flux, such as MPT0L145 in this study, could induce synthetic lethality in cancer cells. Meanwhile, autophagy-related stress response reportedly results in resistance to chemotherapeutic agents and ionizing radiation (10, 11). In bladder cancer, autophagy is related to cancer grade and cisplatin resistance (12–14). Our preliminary data revealed that MPT0L145 sensitizes the efficacy of several autophagy inducers, such as cisplatin, rapamycin, and BGJ398 in bladder cancer cells (Supplementary Fig. S6A–S6C). The autophagy flux was blocked by MPT0L145 as evident by the reversal effects on p62 degradation (Supplementary Fig. S6D). Therefore, it warrants further study on the combination of MPT0L145 and agents that cause prosurvival autophagy to overcome drug resistance.

Earlier studies demonstrate that inhibition of PIK3C3 via gene silencing or a pharmacological inhibitor results in the formation of translucent vacuoles (22, 31). In this study, we observed that MPT0L145 increased large- and phase-lucent vacuoles at the perinuclear region, which were identified as enlarged and alkalinized late-endosomes. Our data suggest that fusion of endosomes and lysosomes is disrupted by MPT0L145, which may explain accumulation of the autophagy substrate p62 (Fig. 1). In fact, PIK3C3 reportedly regulates Rab7 and late endocytic trafficking via recruitment of Armus, the GTPase-activating protein. Knockout of PIK3C3 in mouse embryonic fibroblasts resulted in Rab7 hyperactivation, leading to the failure of intraluminal vesicle formation and lysosomal maturation (37). These results strongly support our observation, and it is worthy to examine the effect of MPT0L145 on Rab7 activity in the future.

Intracellular vacuolization is associated with nonapoptotic cell death processes, such as methuosis, oncosis, paraptosis, and necroptosis (38), but the underlying mechanisms remain elusive. In this study, TEM analysis disclosed enlarged vacuoles with compressed nuclei and swelling of mitochondria (Fig. 2C). Our data also suggested that MPT0L145 promoted mitochondrial dysfunction via measuring OCR (Fig. 5A and D) and a dramatic increase in total and mitochondrial ROS accumulation (Fig. 5B–F). Moreover, MPT0L145 enhanced expression of the DNA damage marker, γH2AX, in a concentration- and time-dependent manner (Fig. 5G). Enforced expression of PIK3C3 rescued MPT0L145-induced cell death (Fig. 4B), γH2AX level (Fig. 5H) as well as ROS production (Fig. 5I and J). Accordingly, we propose that MTP0L145 increases intracellular/mitochondrial ROS production and DNA damage, which, at least in part, contributes to vacuolization-associated cell death (Fig. 6F).

In conclusion, we identified that MPT0L145 is a first-in-class compound, functioning as a dual inhibitor of PIK3C3 and the FGFR pathway. Our findings provide an innovative strategy utilizing a single compound to increase autophagy as the bait, but perturb autophagy flux that promotes bladder cancer cell death via vacuolization.

Disclosure of Potential Conflicts of Interest

No potential conflicts of interest were disclosed.

Authors' Contributions

Conception and design: C.-H. Chen, C.A. Changou, Y. Yen
Development of methodology: C.-H. Chen, C.A. Changou, C.-Y. Chu, H.-C. Wang, Y. Yen
Acquisition of data (provided animals, acquired and managed patients, provided facilities, etc.): C.-H. Chen, C.A. Changou, Y.-C. Lee, C.-Y. Chu, Y.-C. Lin, Y.-R. Liu
Analysis and interpretation of data (e.g., statistical analysis, biostatistics, computational analysis): C.-H. Chen, Y.-C. Lee, K.-C. Hsu, Y.-C. Lin, Y.-N. Lo, Y. Yen

Writing, review, and/or revision of the manuscript: C.-H. Chen, C.-Y. Chu, Y. Yen
Administrative, technical, or material support (i.e., reporting or organizing data, constructing databases): T.-H. Hsieh, H.-C. Wang, Y.-R. Liu, J.-P. Liou
Study supervision: Y. Yen

References

1. Torre LA, Bray F, Siegel RL, Ferlay J, Lortet-Tieulent J, Jemal A. Global cancer statistics, 2012. CA Cancer J Clin 2015;65:87–108.
2. Siegel RL, Miller KD, Jemal A. Cancer statistics, 2017. CA Cancer J Clin 2017;67:7–30.
3. Knowles MA, Hurst CD. Molecular biology of bladder cancer: new insights into pathogenesis and clinical diversity. Nat Rev Cancer 2015; 15:25–41.
4. Ghasemzadeh A, Bivalacqua TJ, Hahn NM, Drake CG. New strategies in bladder cancer: a second coming for immunotherapy. Clin Cancer Res 2016;22:793–801.
5. Boya P, Reggiori F, Codogno P. Emerging regulation and functions of autophagy. Nat Cell Biol 2013;15:713–20.
6. Ktistakis NT, Tooze SA. Digesting the expanding mechanisms of autophagy. Trends Cell Biol 2016;26:624–35.
7. Lamb CA, Yoshimori T, Tooze SA. The autophagosome: origins unknown, biogenesis complex. Nat Rev Mol Cell Biol 2013;14: 759–74.
8. Huang J, Klionsky DJ. Autophagy and human disease. Cell Cycle 2007; 6:1837–49.
9. Yang ZJ, Chee CE, Huang S, Sinicrope FA. The role of autophagy in cancer: therapeutic implications. Mol Cancer Ther 2011;10: 1533–41.
10. Sui X, Chen R, Wang Z, Huang Z, Kong N, Zhang M, et al. Autophagy and chemotherapy resistance: a promising therapeutic target for cancer treatment. Cell Death Dis 2013;4:e838.
11. Kondo Y, Kanzawa T, Sawaya R, Kondo S. The role of autophagy in cancer development and response to therapy. Nat Rev Cancer 2005; 5:726–34.
12. Ojha R, Singh SK, Bhattacharyya S, Dhanda RS, Rakha A, Mandal AK, et al. Inhibition of grade dependent autophagy in urothelial carcinoma increases cell death under nutritional limiting condition and potentiates the cytotoxicity of chemotherapeutic agent. J Urol 2014;191: 1889–98.
13. Lin YC, Lin JF, Wen SI, Yang SC, Tsai TF, Chen HE, et al. Inhibition of high basal level of autophagy induces apoptosis in human bladder cancer cells. J Urol 2016;195(4 Pt 1):1126–35.
14. Lin JF, Lin YC, Tsai TF, Chen HE, Chou KY, Hwang TI. Cisplatin induces protective autophagy through activation of BECN1 in human bladder cancer cells. Drug Des Dev Ther 2017; 11:1517–33.
15. Vanhaesebroeck B, Guillermet-Guibert J, Graupera M, Bilanges B. The emerging mechanisms of isoform-specific PI3K signalling. Nat Rev Mol Cell Biol 2010;11:329–41.
16. Backer JM. The regulation and function of class III PI3Ks: novel roles for Vps34. Biochem J 2008;410:1–17.
17. Futter CE, Collinson LM, Backer JM, Hopkins CR. Human VPS34 is required for internal vesicle formation within multivesicular endosomes. J Cell Biol 2001;155:1251–64.
18. Wu YT, Tan HL, Shui G, Bauvy C, Huang Q, Wenk MR, et al. Dual role of 3-methyladenine in modulation of autophagy via different temporal patterns of inhibition on class I and III phosphoinositide 3-kinase. J Biol Chem 2010;285:10850–61.
19. Yap TA, Bjerke L, Clarke PA, Workman P. Drugging PI3K in cancer: refining targets and therapeutic strategies. Curr Opin Pharmacol 2015;23:98–107.
20. Miller S, Tavshanjian B, Oleksy A, Perisic O, Houseman BT, Shokat KM, et al. Shaping development of autophagy inhibitors with the structure of the lipid kinase Vps34. Science 2010;327:1638–42.
21. Workman P, van Montfort RL. Unveiling the secrets of the ancestral PI3 kinase Vps34. Cancer Cell 2010;17:421–3.
22. Ronan B, Flamand O, Vescovi L, Dureuil C, Durand L, Fassy F, et al. A highly potent and selective Vps34 inhibitor alters vesicle trafficking and autophagy. Nat Chem Biol 2014;10:1013–9.
23. Pasquier B. SAR405, a PIK3C3/Vps34 inhibitor that prevents autophagy and synergizes with MTOR inhibition in tumor cells. Autophagy 2015;11:725–6.
24. Chen CH, Liu YM, Pan SL, Liu YR, Liou JP, Yen Y. Trichlorobenzene-substituted azaaryl compounds as novel FGFR inhibitors exhibiting potent antitumor activity in bladder cancer cells in vitro and in vivo. Oncotarget 2016;7:26374–87.
25. Huang CY, Chen JY, Wu JE, Pu YS, Liu GY, Pan MH, et al. Ling-Zhi polysaccharides potentiate cytotoxic effects of anticancer drugs against drug-resistant urothelial carcinoma cells. J Agric Food Chem 2010;58: 8798–805.
26. Changou CA, Chen YR, Xing L, Yen Y, Chuang FY, Cheng RH, et al. Arginine starvation-associated atypical cellular death involves mitochondrial dysfunction, nuclear DNA leakage, and chromatin autophagy. Proc Natl Acad Sci U S A 2014;111:14147–52.
27. Hsu KC, Chen YF, Lin SR, Yang JM. iGEMDOCK: a graphical environment of enhancing GEMDOCK using pharmacological interactions and post-screening analysis. BMC Bioinformatics 2011;(12 suppl 1):S33.
28. Lee CH, Lee YC, Lee YL, Leu SJ, Lin LT, Chen CC, et al. Single chain antibody fragment against venom from the snake Daboia russelii formosensis. Toxins (Basel). 2017;9:pii: E347.
29. Scott CC, Vacca F, Gruenberg J. Endosome maturation, transport and functions. Semin Cell Dev Biol 2014;31:2–10.

30. Huotari J, Helenius A. Endosome maturation. EMBO J 2011;30: 3481–500.
31. Johnson EE, Overmeyer JH, Gunning WT, Maltese WA. Gene silencing reveals a specific function of hVps34 phosphatidylinositol 3-kinase in late versus early endosomes. J Cell Sci 2006;119 (Pt 7):1219–32.
32. Dall'Armi C, Devereaux KA, Di Paolo G. The role of lipids in the control of autophagy. Curr Biol 2013;23:R33–45.
33. Pasquier B. Autophagy inhibitors. Cell Mol Life Sci 2016;73: 985–1001.
34. Peyraud F, Cousin S, Italiano A. CSF-1R inhibitor development: current clinical status. Curr Oncol Rep 2017;19:70.
35. Chen Y, Xie X, Li X, Wang P, Jing Q, Yue J, et al. FGFR antagonist induces protective autophagy in FGFR1-amplified breast cancer cell. Biochem Biophys Res Commun 2016;474:1–7.
36. Yuan H, Li ZM, Shao J, Ji WX, Xia W, Lu S. FGF2/FGFR1 regulates autophagy in FGFR1-amplified non-small cell lung cancer cells. J Exp Clin Cancer Res 2017;36:72.
37. Jaber N, Mohd-Naim N, Wang Z, DeLeon JL, Kim S, Zhong H, et al. Vps34 regulates Rab7 and late endocytic trafficking through recruitment of the GTPase-activating protein Armus. J Cell Sci 2016;129:4424–35.
38. Maltese WA, Overmeyer JH. Methuosis: nonapoptotic cell death associated with vacuolization of macropinosome and endosome compartments. Am J Pathol 2014;184:1630–42.